Geology 394H 4.15.2014

Variations in magma supply along ${\sim}900~km^2\,of$ the Mid-Atlantic Ridge at $16.5^{o}N$

Will Junkin

Advisors: Laurent Montesi, Wen-lu Zhu, Debbie Smith

Abstract

Small scale (10-1000 m) volcanic edifices present in bathymetric maps of midoceanic ridges (MORs) can be used to investigate spreading mechanisms and spatiotemporal variations in magma supply to the ridge. Geographic Information Systems (GIS) integrate bathymetry data with interpretations of seafloor morphology at multiple scales, enabling a quantitative analysis of the volumes of volcanic edifices and the spatial distributions of these volumes. A morphological analysis was performed on four sets of high-resolution (~0.5 m) bathymetry maps located within ~40 km along the Mid-Atlantic Ridge (MAR) around 16.5°N. Bathymetry data were collected by the Autonomous Underwater Vehicle (AUV) Sentry during an expedition to the MAR in May 2013. The study has two objectives. First, to document any variation in the volcanic and tectonic budget with respect to distance from the axis. "Standard" spreading models predict that tectonic strain should increase away from the axis—but this relation may not be valid above an oceanic core complex, which is suspected to be present in the area of study. Second, the project addresses the relative importance of volcanism between the four areas of high-resolution bathymetric coverage. An analysis in ArcMAP and Fledermaus GIS programs shows that rates of volcanic extrusion have varied over time along the ridge, and that volcanic extrusion generally increases in magnitude from north to south along the ridge. According to previous work on MORs, the long-lived detachment faults in central and southern locations in the area of study should indicate amagmatic spreading, and the absence of such faults in the northern locations should indicate magmatic spreading. However, given that volcanic extrusion rates are a reliable proxy for magma supply beneath the ridge, the results of this study reveal that there is a greater magma supply in the south than in the north. Results of this study also reveal that magma supply along the ridge has not remained constant over time. These results have important implications for our understanding of mid-oceanic ridges and the balance between tectonic and magmatic spreading mechanisms.

1. Introduction

The lithospheric plates on either side of a slow-spreading (<40 mm/yr) mid-ocean ridge (MOR) diverge primarily as a result of tectonic processes operating far from the ridge itself (Perfit and Chadwick, 1998). The two plates are thinnest and weakest where they meet at MORs; consequently, tensional stresses are enhanced near the axis and generate fissures and normal faults. Buoyant magma stored in chambers beneath the MOR rises up through these faults and fissures and into the spreading zone, relieving the tensional stresses imposed on the plates (Figure 1) (Perfit and Chadwick, 1998). Melt decompresses and interacts with seawater, crystallizes in fissures to form dikes, and a portion extrudes from the seafloor to form volcanic edifices (Smith and Cann, 1993; Colman et al., 2012).

As it crystallizes, the magma forms new oceanic crust which, according to the "standard" model of seafloor spreading (Figure 2a), accretes to the two diverging plates in equal amounts (Buck et al., 2005). Also according to the "standard" model, faults typically nucleate near or within axial volcanic ridges, with fault displacement increasing proportionally with distance from the axis (Smith and Cann., 1993). This mode of accretion results in bathymetry that is symmetrical with respect to the ridge axis. The discovery in the 1950s of these symmetricallyspreading, magmatically-active ridges revolutionized the earth sciences: they not only evidenced the existence and relative motions of tectonic plates; but they also accounted for how new lithosphere forms as plates diverge (Nicolas, 1995).

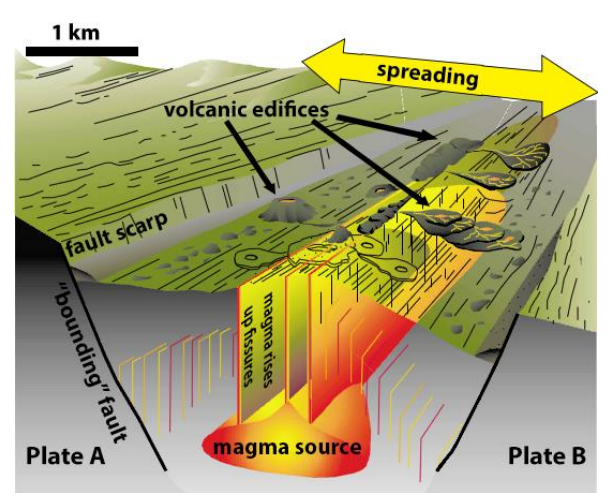


Figure 1: magma in the spreading zone of a midocean ridge (MOR) accretes to both plates as it rises up a fissure, then extrudes from the seafloor to form volcanic edifices. (Adapted from Smith and Cann, 1999)

Surveys conducted in the 1980s and 1990s mapped MORs to far greater extent and detail than previously possible. The resulting maps demonstrated that at slow-spreading ridges such as the Mid-Atlantic Ridge (MAR), as much as half of spreading is actually asymmetrical (Figure 2) (Escartin et al., 2008). Numerical models have suggested that, unlike symmetrical spreading, asymmetrical spreading occurs during periods of reduced magma supply beneath the ridge (Buck et al., 2005; Tucholke et al., 2008). In these circumstances, tensional stresses will be relieved primarily by lithospheric faulting rather than by upwelling of magma. With faulting, the lithosphere thins and stretches, and lithospheric material is extruded onto the seafloor by faults. Individual long-lived faults, called detachment faults, can accommodate up to half of spreading

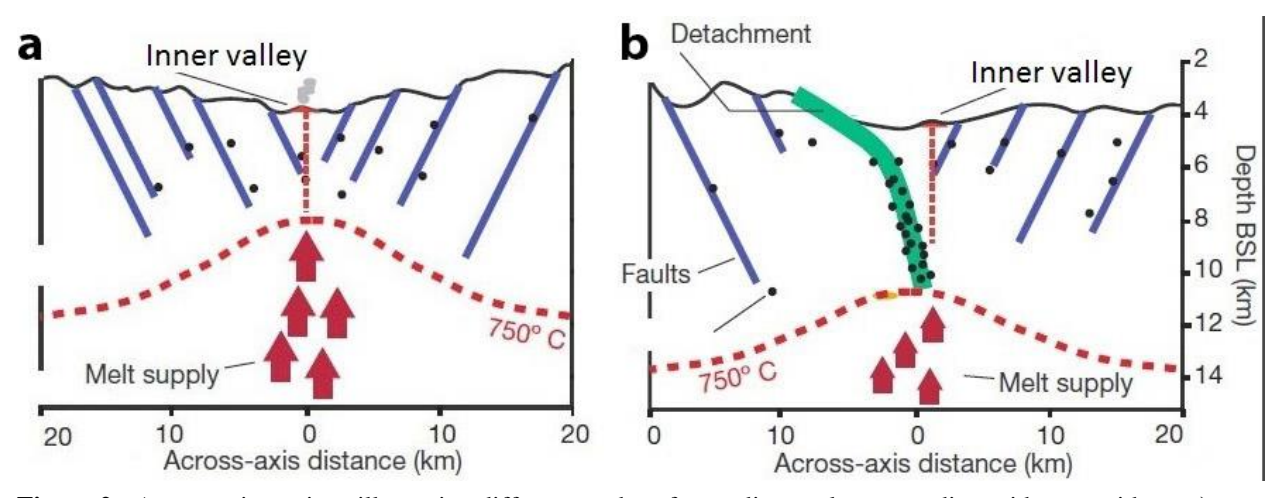


Figure 2: Across axis sections illustrating different modes of spreading at slow-spreading mid-ocean ridges. **a)** With symmetrical spreading, less than 20% of spreading is accommodated by faults, whereas with asymmetric spreading **b)**, a single detachment fault accommodates up to half of spreading. The black dots correspond to earthquakes. (Adapted from Escartin et al., 2008)

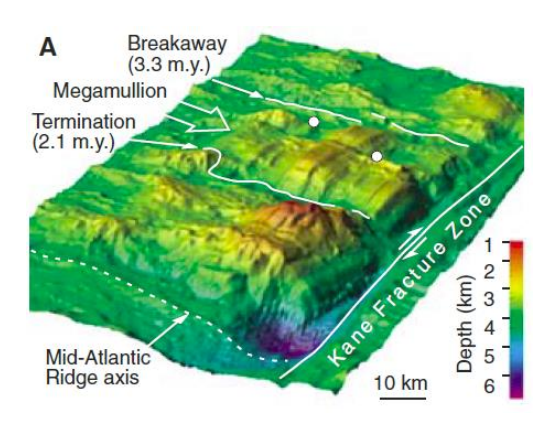


Figure 3: Core complex or alternatively, "megamullion" along the Mid-Atlantic Ridge (Tucholke et al., 2008).

at asymmetric ridges (Figure 2b) (Escartin et al., 2008). In such cases, features called core complexes can form, in which detachment faults sustain kilometers of displacement, exhuming deep crust and sometimes mantle material onto the seafloor (Figure 3) (Tucholke et al., 2008). Accordingly, with asymmetrical spreading, fault displacement does not increase proportionally with distance from the ridge axis.

But much remains unclear concerning asymmetrical spreading, including the subsurface structures of the spreading zone and long-lived detachment faults, why some faults displace kilometers of seafloor while others stop extending after only a short time, and the exact relationship between

detachment fault evolution and magma budget (KN210-05 cruise report).

At a second order scale, ridge segments are defined as large (>30 km) propagating rifts bounded on each end by a transform fault or ridge offset (MacDonald 1991). The bathymetry map in figure 5b contains our area of study and displays second order ridge segmentation, with characteristic ridge axis topographic highs at the segment center and lows at the segment ends. The topography is highest in the segment center because this is where the along-axis lithosphere is thickest and most buoyant. Because magma supply controls lithosphere thickness and buoyancy, it has been inferred that the magma supply is lower at the ends of a second order ridge segment and highest in the center (Neumann and Forsyth, 1993; Thibaud et al., 1998). As a result of this inference, the common occurrence at second order ridge segment ends of long-lived detachment faulting and asymmetric spreading has been cited as evidence that these phenomena are related to a reduced magma supply (Tucholke et al., 2008).

The relationship between spreading symmetry and magma supply can be further illuminated by analyzing seafloor bathymetry at a much finer scale than second order ridge segments. Individual seafloor faults and volcanic edifices can be used to infer magma supply, with heavily faulted areas indicating a lower magma supply,

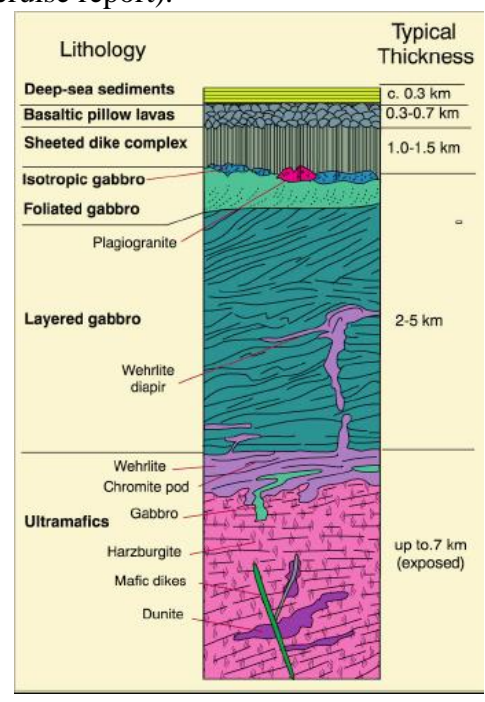


Figure 4: Synthetic ophiolite stratigraphic column showing a volumetric ratio of volcanic (basaltic pillow lavas) material to magmatic (sheeted dike complex and gabbro layers) material of ~1:10 (from Nicolas and Boudier, 2003)

and areas covered by volcanic edifices indicating a higher magma supply. A quantitative approach can be taken based on the volumetric proportion of volcanic to magmatic material observed in ophiolites (figure 4). Assuming this proportion is constant in the area of study of this project, volcanic volumes can be used as a proxy for magma supply (Perfit and Chadwick, 1998).

Consequently, an analysis of the volumes and spatial distribution of volcanic edifices can be used to estimate spatial and temporal variations in magma supply. Seafloor morphology can then be compared with variations in local sediment thicknesses to estimate the relative time that a fault surface or volcanic feature has been exposed on the seafloor (KN210-05 cruise report; KN210-05 newsletter).

Regional bathymetry data sets gathered during the KN 210-05 cruise (Smith et al., 2013), the AT04L04 cruise (2001, unpublished data), the KN161L04 cruise (2000, unpublished data), and by Fujiwara et al. (2003), reveal variation in along-axis depth (Figure 5b-d), suggesting variable magma budgets along-axis. Bathymetry data sets also reveal asymmetric spreading characterizing the area of study, manifested in part by two parallel linear ridges on the western flank of the axis (Figure 5c). These apparently tectonic ridges have been interpreted as the rotated tops of detachment faults (Smith et al., 2008), an indication of amagmatic spreading. This hypothesis is supported by hydroacoustic sensor data from the area of study, which records the high rate of seismicity characteristic of tectonic spreading (Smith et al., 2003; Escartin et al., 2008). The area of study was chosen based on the interpretations that the east and west ridges in figure 5 represent progressive stages of development of a long-lived detachment fault, and that the corrugated surface in figure 5c overlies a core complex produced by this long-lived detachment fault development. Testing these hypotheses, investigating along-axis fault linkages, fault activity, and the relationship between fault development and magma supply were the purpose of the KN 210-05 research cruise (KN210-05 newsletter).

The importance of understanding spreading and magmatic processes at MORs extends far beyond satisfying curious marine geologists. Though it is mostly hidden beneath kilometers of water, the oceanic lithosphere plays as important a role in society and geology story as its continental counterpart. The lithosphere forming at MORs is the same material that subducts under populated landmasses, influencing the formation of mineral deposits and causing earthquakes and volcanoes. We cannot predict these societally impactful phenomena until we fully understand the character of the subducting material, including the circumstances of that material's origin at MORs. Moreover, core complexes at MORs are one of the few places on earth that can expose the mantle (Tucholke et al., 2008), and MOR volcanism directly samples mantle melt (Perfit and Chadwick, 1998). Understanding the mantle requires that we collect samples from all available sources, and that we understand the mechanisms by which those sources emerge and evolve. Finally, alteration of the mantle and dissolution of ions by hydrothermal activity directly influence the chemistry of the oceans and the solid earth (Staudigel 2013), as well as determine the conditions that support communities of chemosynthetic biological organisms (Buck et al., 2005). To better understand the chemical evolution of the seawater and solid earth reservoirs, and perhaps to illuminate the origin of life itself, we must continue to investigate spreading at MORs.

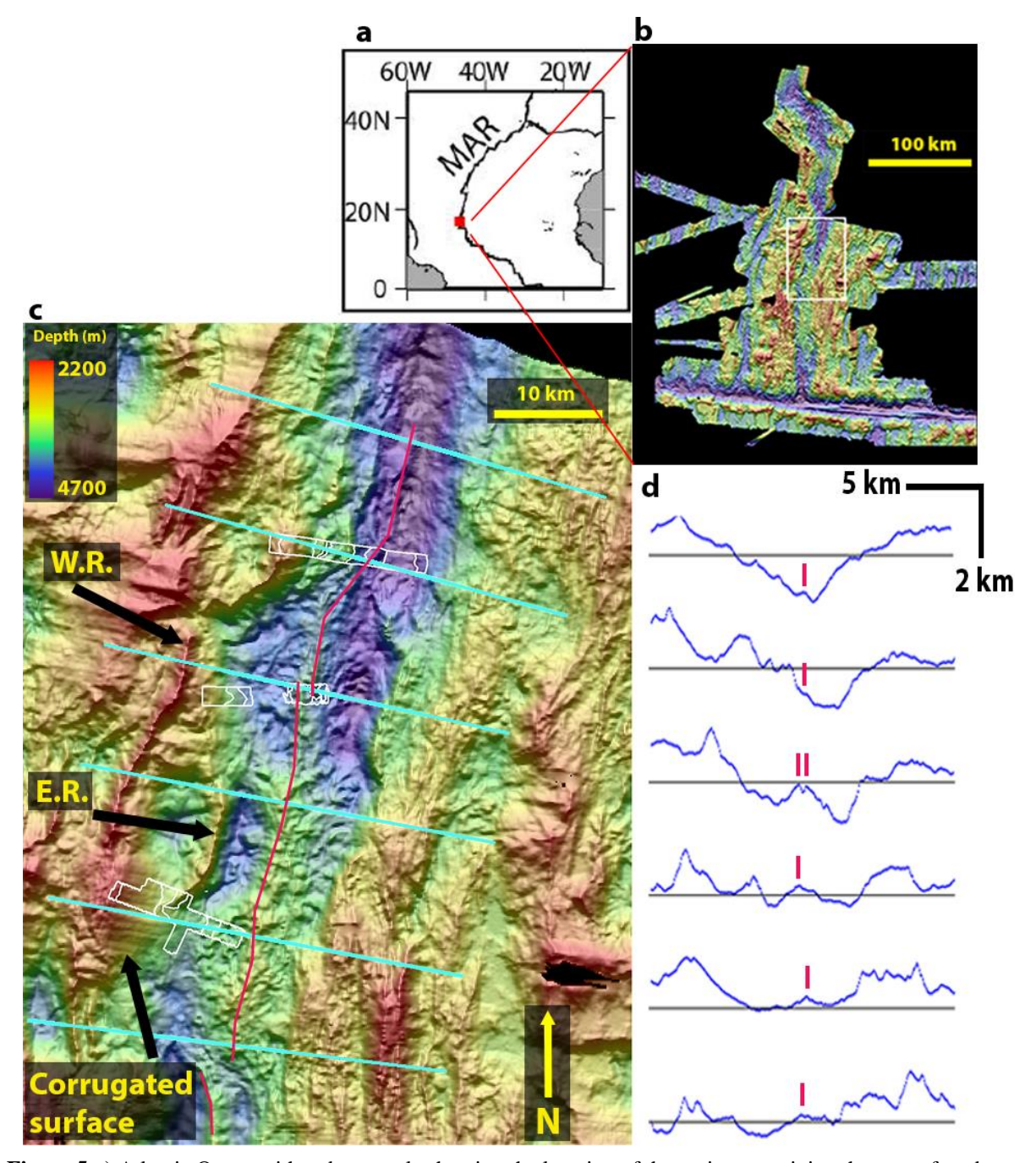


Figure 5 a) Atlantic Ocean with red rectangle showing the location of the region containing the area of study. **b**) Regional bathymetry map with area of study bounded by white rectangle. Map shows 2nd order ridge segment bounded by transform fault in the south, offset ridge in the north. **c**) Asymmetric ridge in area of study. The red lines in the center of the image approximate the ridge axis. The white lines bound areas for which *Sentry* gathered high-resolution bathymetry data. East Ridge (E.R.) and West Ridge (W.R.) are interpreted to be the rotated tops of detachment faults, a manifestation of the tectonic activity of the region. The corrugated surface is indicative of a long-lived detachment fault forming a core complex. **d**) Profiles of the ridge and inner valley taken along the blue lines in c). The black horizontal lines are at 3500 m depth, the red lines approximate the horizontal location of ridge axis. Note the increase in ridge axis elevation from north to south.

2. Objectives of research

The purpose of this project is to investigate how, within a segment of the MAR centered at 16.5°N, magma supply has varied along the ridge axis and through time. Regional bathymetry data show a marked increase in ridge elevation from north to south along-axis (Figure 5), which indicates a thickening crust and consequently an increasing magma supply from north to south. Neumann and Forsyth, 1993; Thibaud et al., 1998). High-resolution bathymetry gathered on the KN210-05 research cruise by the Autonomous Underwater Vehicle (AUV) Sentry reveal significant volcanic coverage of the north, central, and south areas of the area of study, and all areas appear to contain abundant faulting. To investigate how the area of study conforms to modern theories of seafloor spreading, I hypothesize that a detailed analysis of small-scale (10¹-10² m) volcanic edifices present in high-resolution bathymetry maps of the area of study will reflect along the ridge: 1) increasing magma supply from north to south, and 2) time-invariant magma supply. By defining geo-referenced polygons around the perimeters of volcanic edifices and then extracting values for base area and mean depth, eruptive volumes of volcanic events can be estimated. In conjunction with eruptive ages estimated from relative sediment thicknesses, the spatial distribution and volumes of volcanic events can be used to interpret magma supply over time at a ridge (Perfit and Chadwick, 1998). Combined, these analyses provide a detailed perspective into the magmatic and tectonic processes at this location on the MAR. From this approach it is possible to evaluate the processes controlling whether spreading is symmetrical or asymmetrical, magmatic or amagmatic, and to generalize these observations and their implications for exposures of mantle at the seafloor to the global MOR system.

3. Hypotheses

- 1. Magma supply increases from north to south along-axis, concomitant with increase in seafloor height from north to south along-axis. Accordingly, volcanic spreading dominates in the north, tectonic spreading dominates in the south.
- 2. Within ~10⁶ yrs required to build a MOR inner valley, magma supply at the axis has remained constant over time. Accordingly, fault-accommodated strain should increase progressively away from the ridge axis, and volcanic volumes should remain constant.

4. Experimental Design

4.1. Data collection

Data was collected aboard the Research Vessel *Knorr* operating out of Woods Hole, MA (KN 210-05 research cruise). We investigated ~900 km² of seafloor centered on the ridge at 16.5° N, taking photographs with a TowCam camera system towed at the seafloor (Figure w), collecting samples, measuring seawater chemistry, and gathering gravity, magnetic, sub-bottom profile, and low- and high-resolution bathymetry data. I participated significantly with all the different data collection methods.

Primary data analyzed in this study originate from two systems employed during the KN210-05 research cruise. Low-resolution regional bathymetry data were gathered by hull-mounted "Seabeam sonar." This system produces ~10 km-long lines of bathymetry data (line length varies with depth). Lines of data run perpendicular to the ship's keel; multiple lines collected by a moving ship are combined to produce elongate "swaths" of bathymetry data. Each line has a spatial resolution of ~150 m (spatial resolution varies with depth and ship

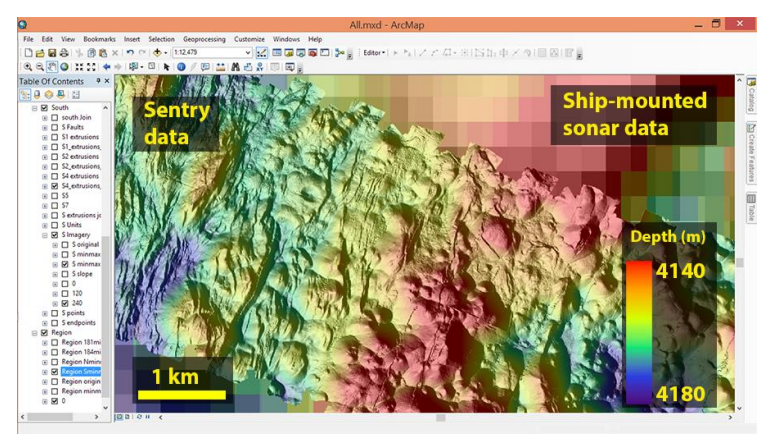


Figure 6: high-resolution (~0.5 m) bathymetry data collected by *Sentry* overlaid on low-resolution (~150 m) bathymetry data collected directly from R.V. *Knorr*. Data visualized in ArcGIS with partially transparent depth color ramp overlying shaded relief map.

speed). The spatial resolution of a line is the minimum distance over which the instrument measures a single depth. Regional bathymetry data is used mainly to provide a regional context to the high-resolution dataset next described. No detailed morphological analysis will be conducted using the Seabeam regional bathymetry. High-resolution bathymetry data (Figure 6) were gathered during seafloor dives by the Autonomous Underwater Vehicle *Sentry* (Figure 7). *Sentry* can operate at up to 6000 m of depth, can self-navigate over extremely variable undersea terrain, and can operate at ~4000 m for up to 24 hrs. Over the course of each dive, *Sentry* "flew" at a height of approximately 60 m above the seafloor measuring lines of bathymetry data oriented perpendicular to its keel. At this height, and at a speed of ~1 m/s, *Sentry's* Reson 7125 multibeam sonar package recorded a maximum useful line of bathymetry data 180 m-wide with a spatial resolution of 0.25 m. Given this line width, an average speed of 1 m/s, and ~20 hrs spent collecting data at the seafloor, *Sentry* was able to trace an assigned "trackline" to produce ~3.4 km² of bathymetry data per dive (Sentry dive summaries). Raw bathymetry data was downloaded from *Sentry* after each dive. The distance and angle from which acoustic signals from *Sentry*



Figure 7: Autonomous Underwater Vehicle (AUV) *Sentry* retrieved after a dive on research cruise KN 210-05

arrived at the ship were combined with inertial sensors and Doppler velocity log sonar systems onboard *Sentry* to calculate the position of *Sentry* relative to the *Knorr* over time. The position of the *Knorr* was determined via Global Positioning Systems (GPS). Aboard the ship, the technical team for *Sentry* combined *Sentry* sonar data, *Sentry*-ship acoustic transmissions, and ship Global Positioning System (GPS) data gathered during multiple dives to produce the bathymetry data around which this project is based.

I received bathymetry data in the form of five netCDF grid files. The files contain x (decimal degrees longitude), y (decimal degrees latitude), and z (m) values describing the locations in three dimensions of each of the pixels contained on a map. One netCDF file contains the regional bathymetry data

gathered from ship-mounted sonar, and the other four files each contain a high-resolution bathymetry data set collected by *Sentry* (Figure 5): one from the north of the area of study, two from the center, and one from the south.

4.2. Visualizing bathymetry in ArcMAP

I used the *ArcMAP* 10.1 and *Fledermaus* GIS platforms to estimate the base areas and the minimum (deepest) and mean depths of the surfaces of volcanic edifices user-defined within the two high-resolution maps. I will describe the steps involved in this process.

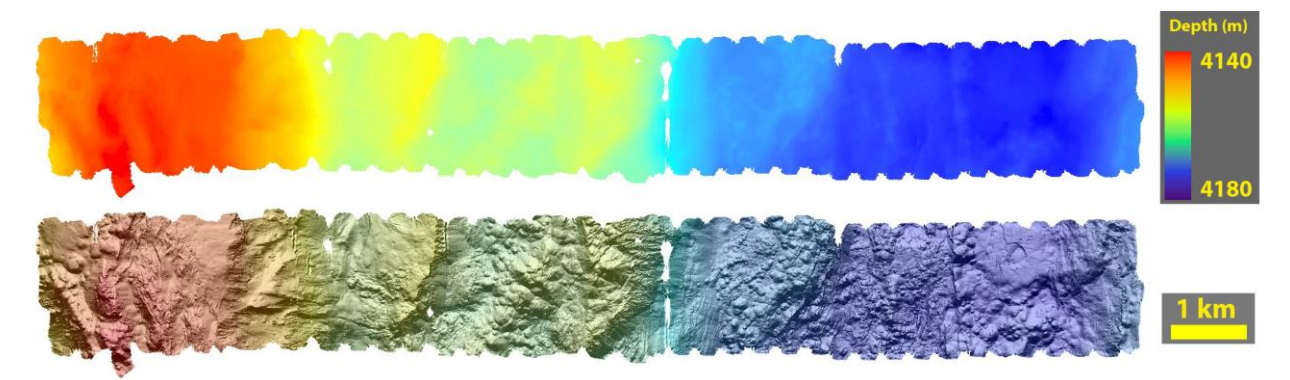


Figure 8: top) from the north swath, netCDF raster layer with color ramp indicating bathymetry; **bottom)** netCDF raster layer set to 70% transparency and overlayed on a shaded relief layer

To begin, the data needed to be converted to a COARDS-compliant format. This was achieved using the Generic Mapping Toolbox command grdreformat. For the area 184 grid file, the command becomes: grdreformat sentry184 20130617.grd sentry184.grd. Similar commands where used for the other grid files. I specified the coordinate system for the ArcMAP data frame (main window). The netCDF files are based on the geographic coordinate system "World Geodetic Survey (WGS) 1984," but ArcMAP can only extract area from a flat surface, so data must be plotted on a projected coordinate system. With this in mind, I chose to base the ArcMAP data frame on the projected coordinate system "WGS 1984 World Mercator." I set the data frame display units to m. In the "make netCDF raster layer" tool, I uploaded the netCDF file, specifying bathymetry (z) as the "variable," longitude as the "x dimension," and latitude as the "v dimension." The output raster layer visualizes the bathymetry data in the ArcMAP window by displaying different depths in different colors (Figure 8). But individual volcanic edifices rarely show up on such a map, as the vertical scale of individual edifices differs from the vertical scale of the complete bathymetry map by orders of magnitude.

To visualize individual volcanic edifices, in the image analysis window I inputted the raster layer into the "hillshade function" to create grayscale shaded relief layers of data. Each layer simulates the shadows cast by bathymetric relief illuminated by an artificial source of light with a 45° elevation. In addition, to convert the elevation units (m) to the horizontal coordinate units of the dataset (decimal degrees), I set the "z factor" at 2e-5. I

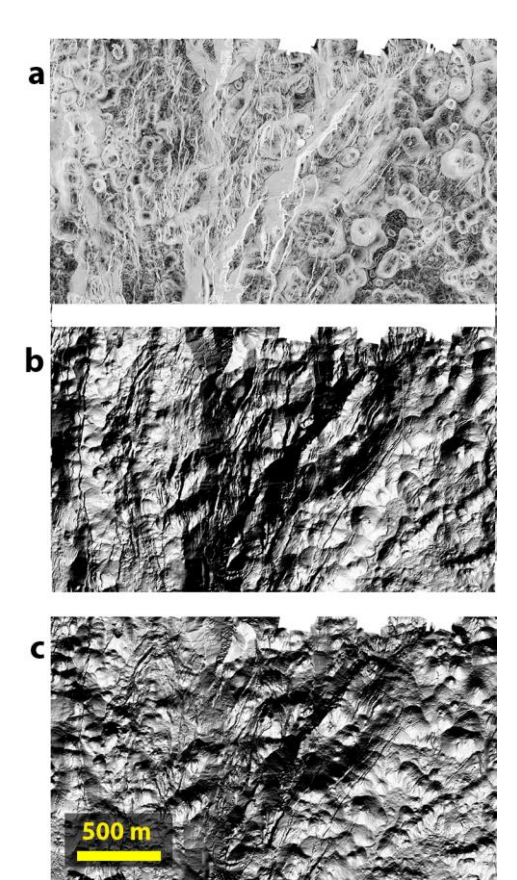


Figure 9: Visualization layers produced in *ArcMAP*. Field of view contains area from units N2 and N3. Different perspectives aid in identification of features and feature dimensions: **a**) slope layer produced by slope function; **b-c**) shaded relief layers produced by hillshade function, with azimuth set at b) 45° and c) 315°

varied the "azimuth" of the light source by 45° increments for each layer (45°, 90°, 135°, etc.). The result was eight layers that simulate light shining on the bathymetry from eight different directions (Figures 9b and 9c).

To further aid in the identification of volcanic edifices, I again used the image analysis window to input the raster layer into the "slope function," which produces a grayscale layer that displays the rate of change of elevation. I set the "output measurement" to "degree," and after experimenting with a variety of values for the "z factor," I chose 4e-5 as the value that best reveals volcanic edifices in the map (Figure 9c).

To best visualize bathymetry at a scale encompassing the entire high-resolution bathymetry map, I set the transparency of the original raster layer to 70% and placed it on top of a shaded relief layer (Figure 8).

4.3. Visualizing bathymetry in Fledermaus

This project relies heavily on the accurate interpretation of (1) which constructs in the bathymetry map are volcanic, and (2) what are the perimeters of those constructs. The nine imagery layers produced in *ArcMAP* were usually sufficient for these interpretations; but in some cases, as when an edifice exhibited particularly low relief or when edifices overlapped, I referred to *Fledermaus* for clarification. *Fledermaus* is a user-friendly, geospatial analysis software package

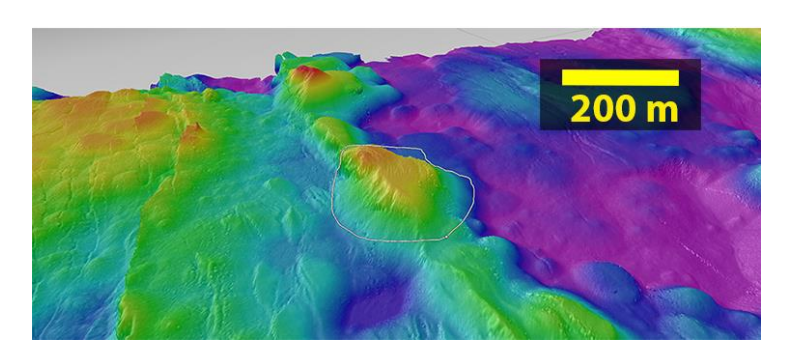


Figure 10 *Fledermaus* oblique perspective of a volcanic edifice in N Swath. 3D perspective of *Fledermaus* can reveal features and feature boundaries difficult to identify in the static perspective of *ArcMAP*

that projects topographic or bathymetric data into an interactive 3D environment (Figure 10). Cross section profiles are also easily produced in *Fledermaus*. More significantly, users can "fly" across landscapes and continuously alter in 3D the perspective from which features are viewed, which provides an intuitive way to understand the geometry of the seafloor topography. For these reasons, *Fledermaus* is superior to *ArcMAP* for identifying volcanic edifices and their dimensions. However, *ArcMAP* imagery analysis is superior for visualizing bathymetric data from a fixed perspective (to which most scientific communication is restricted), and *ArcMAP* offers superior data management and quantitative analysis tools for computing data such as volume. To my knowledge, *ArcGIS* has all the capabilities of *Fledermaus*—profiles can be generated in *ArcMAP* (Figure 5b), and another *ArcGIS* application, *ArcScene*, supports 3D navigation—however, I only rarely required the use of these techniques, and *Fledermaus* is far easier to learn and use quickly than *ArcGIS* applications.

To view bathymetry in *Fledermaus*, I used the application *Magic Hat* of the *Fledermaus* software suite. I uploaded netCDF files as gridded data (.grd format), converted gridded data to scene data (.sd or .scene), then uploaded scene files into *Fledermaus*. I assigned a colormap that best displayed the bathymetry data. To reveal topography further, in the "shading tab, I applied a

shading function and adjusted "specular" to the maximum setting. Throughout the analysis, I readjusted the specular property of the surface, as well as the azimuth and elevation of the shading light source to best visualize the dimensions of volcanic edifices.

4.4. Defining polygons and extracting data in ArcMAP

For each of the high-resolution bathymetry data sets, I uploaded the netCDF file into the "make netCDF table view" tool. This creates a table of the x (longitude), y (latitude), and z (m) attributes of the netCDF file. I "displayed xy data" from these points in the *ArcMAP* window, specifying longitude as the "x field," latitude as the "y field," z as the "z field," and "WGS 1984" as the geographic coordinate system. This creates a layer file with all the points from the table distributed in the *ArcMAP* data frame according to each point's x and y values, with each point retaining but not visualizing its z value.

Features of interest are interactively defined within *ArcMAP* as "polygons." Multiple polygons describing related features form one "polygon shapefile." I based polygon shapefiles on the same projected coordinate system as the *ArcMAP* window, "WGS 1984 World Mercator."

Using the eight shaded relief layers, the slope layer, and where necessary, referring to *Fledermaus*, I defined polygons around what I interpreted to be the perimeters of edifices of volcanic origin. I based these interpretations on morphological descriptions from previous work (Smith and Cann, 1993; Smith et al., 1995; Perfit and Chadwick, 1998; Colman et al., 2012; Searl and Escartin, 2004; Searle et al., 2010). In all, I classified 1396 edifices as "hummocks," "ridges," or "seamounts" (Figures 12-14). I defined hummocks as distinct volcanogenic hills or mounds with rounded horizontal cross sections. In the data sets, four hummock-shaped edifices (one in N2 consisting entirely of a single hummock, the others composed in part of multiple hummocks) stood out as significantly greater in diameter than the other hummocks, and with significantly flatter profiles; I defined these edifices as seamounts. The data sets also contained linear edifices composed in part of distinct hummocks; I defined these edifices as ridges. These definitions are qualitative and subjective, and in classifying volcanic edifices, I relied heavily on examples from the literature.

In addition to defining polygons around volcanic edifices, I defined polygons around what I interpreted to be "units" (Figure 11). I distinguished units based on features visible at the

scale of the high-resolution bathymetry maps, such as fault scarps, ridges, and abrupt changes in seafloor morphology.

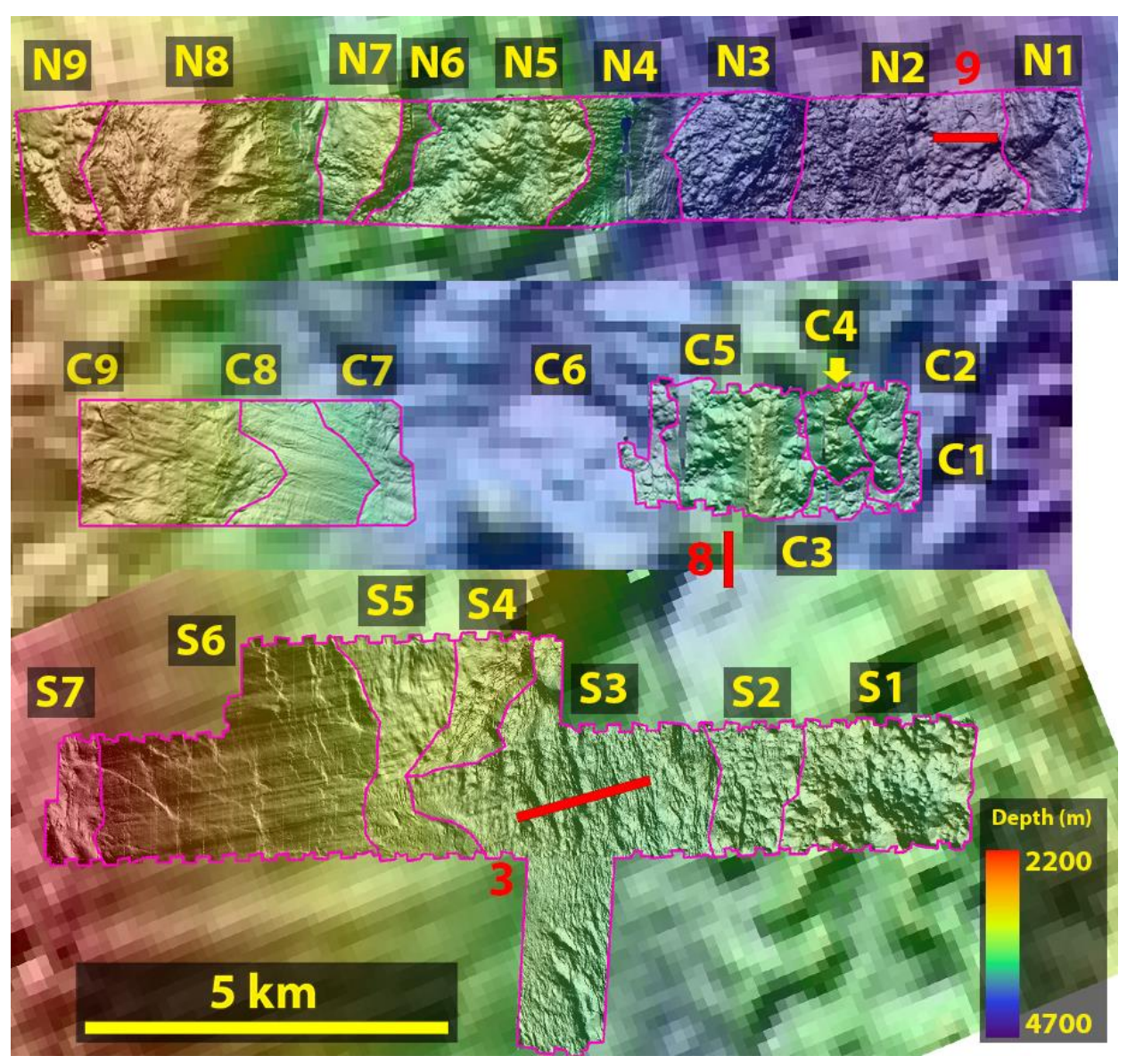


Figure 11: High-resolution bathymetry maps analyzed in this study, with color ramp and shaded relief layers. Units are defined based on features visible at this scale, such as fault scarps, ridges, changes in seafloor morphology, and abrupt changes in slope visible in slope maps (not shown). Map areas are true to scale; orientations of maps and distances between maps have been altered (except C7-C9 and C1-C6 relative to each other). TowCam runs are approximated by red lines.

The purpose of this study is to estimate eruptive volumes, but volume estimates will vary depending on the scale at which edifices are measured. If treated as a single edifice, a ridge or seamount composed of multiple overlapping hummocks will yield a greater volume than if only the hummocks exposed on the surface of the ridge or seamount are considered. While this

volume dependence on edifice scale makes it difficult to determine the absolute volume of material erupted at a given location, relative erupted volumes at various locations along the ridge can still be determined by consistently performing measurements at different scales at each location. To this end, I conducted analyses on four different data sets for each high-resolution bathymetry map. For the respective data sets, I considered volcanic edifices

- 1. distinct hummocks (Figures 12b, 12f, 12j; and 14c)
- 2. ridges as well as distinct hummocks that are not part of a ridge (Figures 12a, 12e, 12i; and 14d)
- 3. seamounts as well as distinct hummocks that are not part of a seamount
- 4. seamounts, ridges, as well as distinct hummocks that are not part of a seamount or ridge

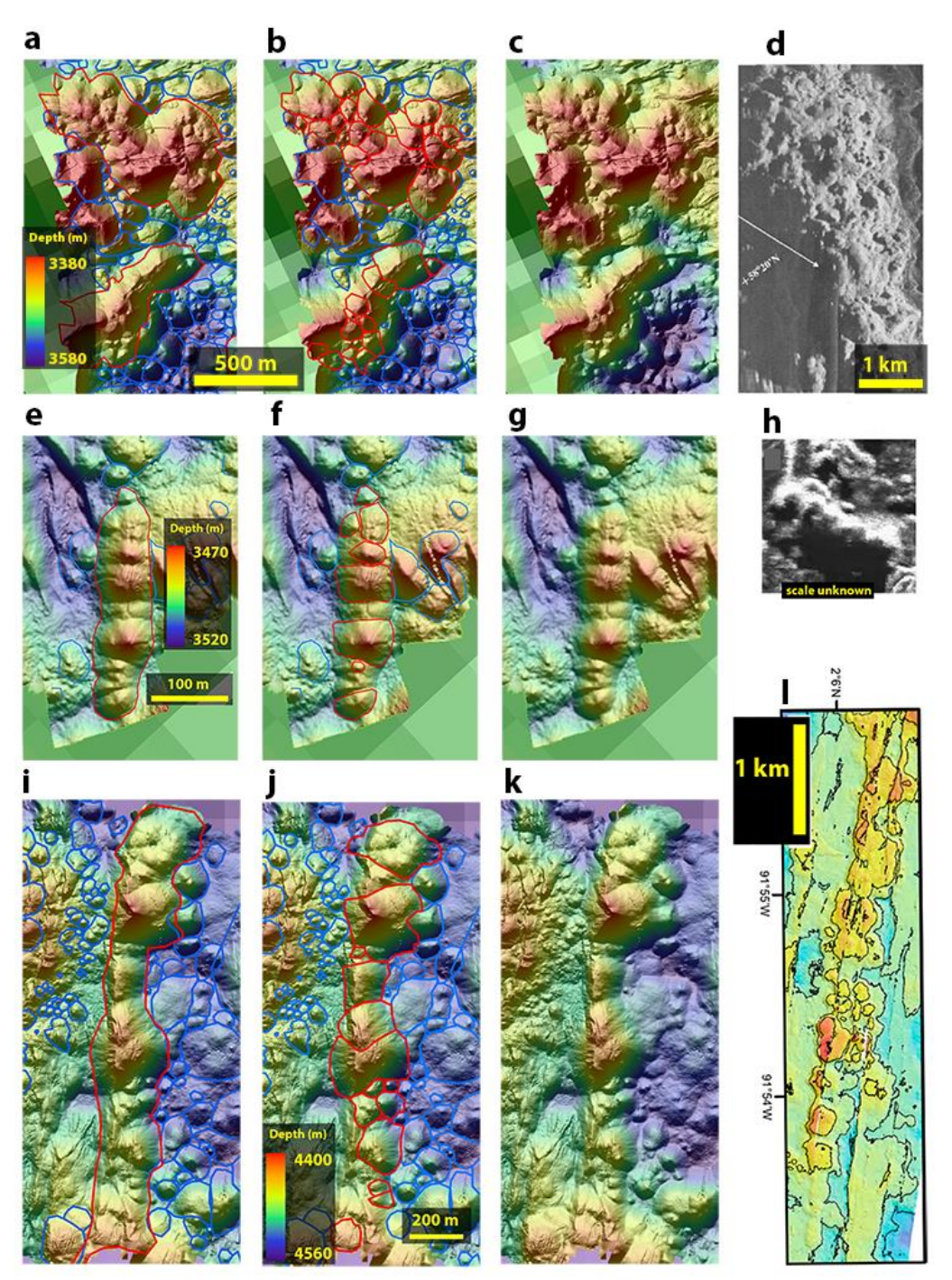


Figure 12: Ridges show a variety of morphologies, but are typically oriented perpendicular to the spreading direction and stress field. Examples of ridges analyzed in this study from unit S1 (a-c), S2 (e-g), and N2 (i-k). **a**), **e**), and **i**) show polygons defining perimeters of distinct hummocks that are not part of a ridge (blue), as well as ridges (red) composed partially of distinct hummocks; **b**), **f**), and **j**) show polygons defining perimeters of distinct hummocks that are not part of a ridge (blue), as well as hummocks that are part of a ridge (red); **c**), **g**), and **k**) show polygons removed. For the ridge(s) from each unit, ridges of similar morphology analyzed in previous studies are shown at right: **d**) from the Reykjanes Ridge (Smith, 1995); h) from the MAR at 45°N (Searle et al., 2010); l) from the Galápagos Spreading Center (Colman et al., 2012)

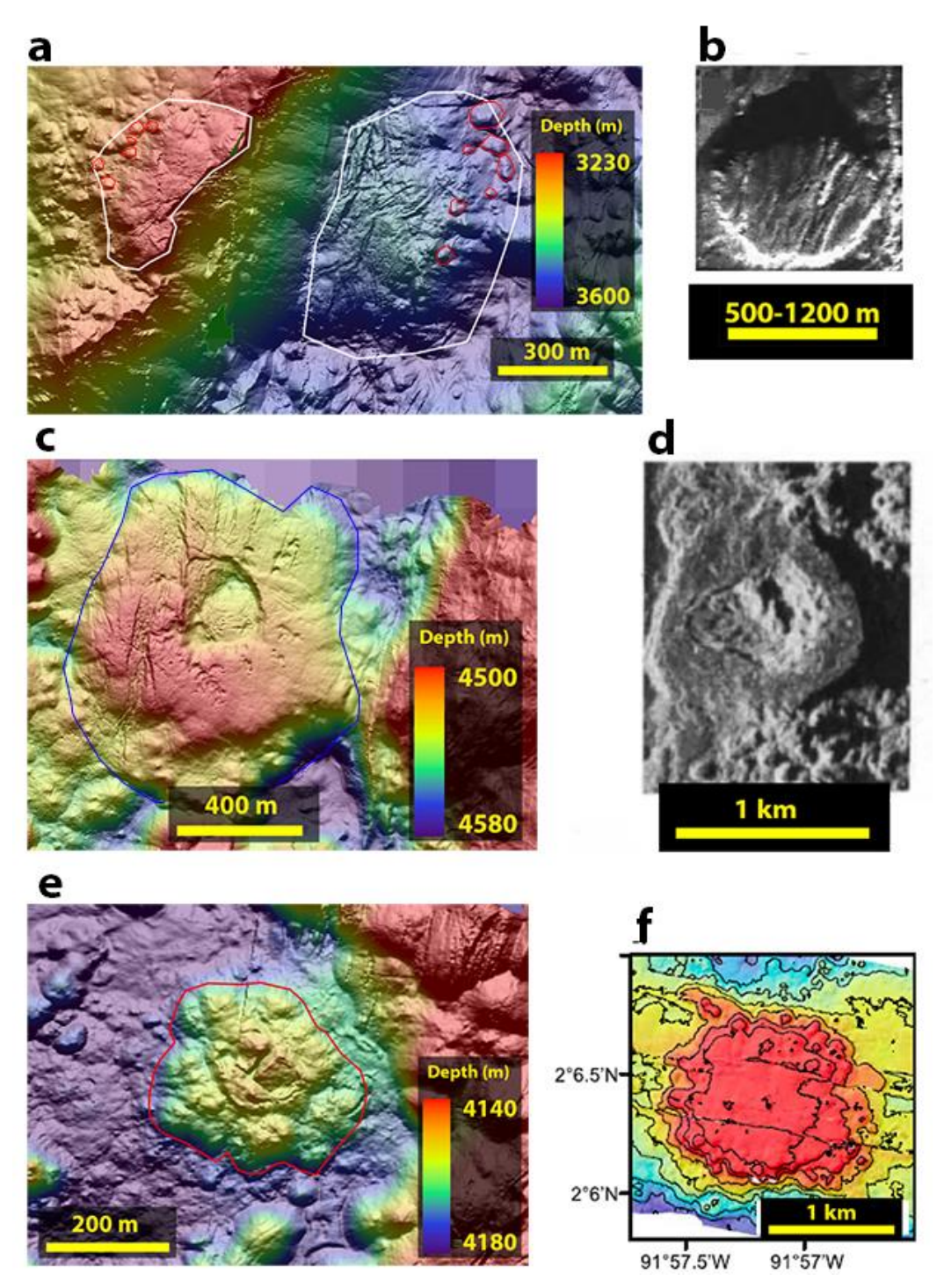


Figure 13: a) single seamount (encircled white) composed in part by distinct hummocks (encircled red) spans N5 and N7, interpreted as having been split in two by faulting (of which the scarp composes N6); b) from the MAR at 45°N (Searle et al., 2010); c) large seamount (circled blue) in N1, with collapsed central crater; d) with collapsed central crater, from the northern MAR (Smith and Cann, 1993); e) seamount (circled red) in N3; f) from the Galápagos Spreading Center (Colman et al., 2012)

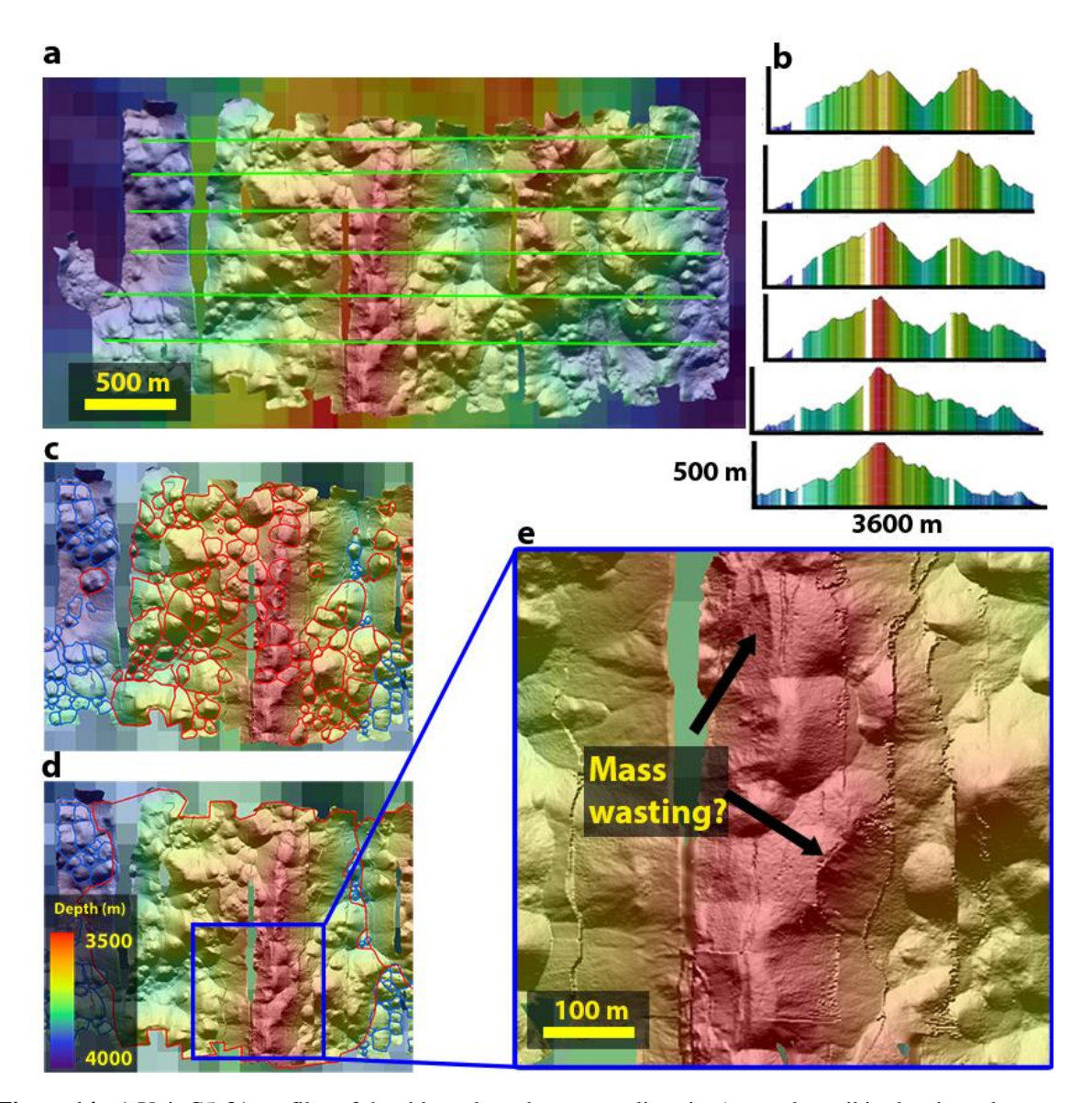


Figure 14: a) Unit C5; **b)** profiles of the ridge taken along green lines in a) reveal a strikingly triangular cross section, possibly a secondary feature caused by erosion of hummocks; **c)** ridge defined in red as individual hummocks; **d)** massive ridge defined in red as one unit; **e)** curved surfaces on summit hummocks indicate mass wasting has reshaped the ridge, an explanation consistent with the triangular cross section of the ridge

I included in the analysis faulted edifices that I could interpret as having once been intact volcanic constructs, so long as I could confidently define their perimeters. I attempted to contain the base areas of the polygons within the rasterized layer; where volcanic edifices are only partially contained within the rasterized layer, they are partially contained within the polygons.

Some units contain no volcanic edifices. Other units likely contain no volcanic edifices; however, because zero is a precise value given the uncertainty involved in how I identify

volcanic edifices, I chose to try and define polygons around possible volcanic edifices in these units.

For each of the four volcanic edifice data sets I defined for each of the four bathymetry maps, I "spatially joined" polygon shapefiles with the xy layers. The spatial join creates a "joined output shapefile." This shapefile records, along with other values, the mean, minimum, and maximum depths (m) of the xy points that fall within the base area of each polygon. These values can be viewed in the attribute table of the shapefile. I added three "fields," or columns to this table and used the "calculate geometry" tool to populate these fields with the base area (m²) of each polygon, and the x coordinate (m) and y coordinate (m) of the centroid of each polygon, respectively. I exported this attribute table as a .txt file for analysis in *Microsoft Excel*.

On the east edge of the bathymetry map, I extracted the x and y coordinates (m) of the endpoints of a line that I defined as running parallel to the ridge axis. I interpreted the orientation of the ridge axis from the regional bathymetry map. For the north swath only, I calculated the distance between the centroid of each polygon and this line to determine the relative distance of each volcanic edifice from the ridge axis (Figure 17).

I created a polyline shapefile with the same coordinate system as the original regional raster, then drew six lines across the inner valley, perpendicular to the ridge. I used the "stack profile" tool (ArcToolbox>3D Analyst Tools>Functional Surface>Stack Profile) to extract x (m) and z (m) values for all the original regional raster pixels that intersect the six lines. The stack profile tool returned these data in table format, which I exported as a .txt file for analysis in *Excel* (Figure 5b).

4.5. Defining profiles and extracting data in Fledermaus

I drew profile lines perpendicular to the spreading axis across the four high-resolution bathymetry maps. *Fledermaus* records x and z values of each point along a user-defined profile line. One point is recorded for each meter of the profile line. Data can be visually observed in *Fledermaus*, or exported to *Excel* for quantitative analysis.

4.6. Analysis in Microsoft Excel

I imported data from *ArcMAP* and *Fledermaus* into *Excel*. *Excel* is useful for organizing data, performing calculations on large data sets, and producing charts and graphs. I performed the following calculations in *Excel*:

(1) Volcanic edifice mean height

For each volcanic edifice, I subtracted the mean depth from a base depth to determine mean height. See uncertainty analysis for details on base depth.

(2) Volcanic edifice volume

For each volcanic edifice, I multiplied base area by mean height to determine volcanic volume. This allows for a comparison of individual volcanic volumes within and between units, as well as a comparison between units of the various totals discussed below ((3)-(5)).

(3) Total volcanic edifice volume

I summed volcanic edifice volumes from each unit to determine total volcanic volume per unit (Figure 18). This allows for a comparison of the volcanic activity between units.

(4) Total volcanic edifice volume per unit area

I divided total volcanic edifice volume per unit by unit area (Figure 19). Normalizing the volcanic volumes by unit area allows for an analysis of volcanic edifice volume that is independent of the unit areas, which are user defined and heavily subject to interpretation.

(5) Total volcanic edifice area per unit area

I divided total volcanic edifice area per unit by unit area (Figure 20). This provides insight into the magma supply of a unit by showing what proportion of a unit is covered in volcanic edifices.

(6) Box and whisker plots

For each unit, I plotted the distribution of individual hummock volumes on a box and whisker plot (Figure 21). For this analysis, only individual hummocks were considered to be volcanic edifices, not ridges or seamounts. The five horizontal lines in each box and whisker plot represent the y-axis value corresponding, from top to bottom, to the 90th, 75th (upper quartile), 50th (median), 25th (first quartile), and 10th percentile datum.

(7) Regional bathymetry profiles

I uploaded the .txt file containing the data exported from *ArcMAP* by the stack profile tool. I plotted depth versus horizontal distance for each of six profile lines (Figure 5d).

4.7. Uncertainty analysis

Uncertainty in the estimation of the spatiotemporal distribution of magma supply is introduced at almost every stage in the analysis. Accordingly, the analysis is meaningless without some quantification of uncertainty. I identified three possible sources of uncertainty in the experimental design:

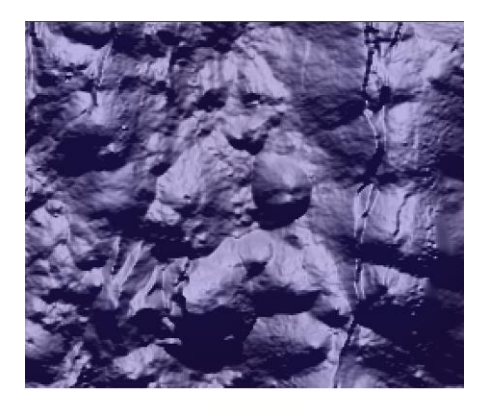
(1) Sentry bathymetry data collection

A small amount of uncertainty was first introduced when *Sentry* measured bathymetry during its dives. Uncertainty results from navigation and bathymetry measurements. The precision of the processed navigation of *Sentry* depends on the precision with which the position of *Sentry* is determined relative to the ship, and the precision with which the position of the ship is determined relative to GPS satellites. *Sentry* navigation precision is usually better than ± 10 m. This is the uncertainty in the position of the entire map; all points within a bathymetric map produced by *Sentry* will be affected by this uncertainty equally and in the same direction. This uncertainty will have no effect on the distance or volume calculations. Points within a bathymetric map produced by *Sentry* will have some uncertainty relative to each other. In addition, bathymetry measurements by *Sentry* introduce uncertainty. But these sources of uncertainty are negligible when compared to the sources described in the next section (D. R. Yoerger, personal communication).

(2) Volcanic edifice volume calculations

The greater source of uncertainty in the analysis derives from how I determine the base area and mean height, and from these, the volume of each volcanic edifice present in the bathymetry data. This uncertainty derives from three sources:

- (i) Interpretation of bathymetry: the first source of error in the analysis is the interpretation of volcanic edifices from bathymetry data. This interpretation is subjective and extremely difficult to quantify; I have minimized the effect of this uncertainty by spending many hours with my various advisors reviewing and discussing interpretations.
- (ii) User-defined polygon perimeters: The second source of error in the analysis is the definition, by me, of the perimeter of each polygon. To estimate the uncertainty caused by the perimeter definitions, I compared the volumes calculated from a variety of polygon definition methods. Polygons chosen for comparison include:
 - 1. A 24-sided polygon, a 16-sided polygon, and an 8-sided polygon, all of which I neither carefully nor carelessly defined around a reference volcanic edifice displayed at a scale of 1:3000, first in the shaded relief map with azimuth of 0°, then with an azimuth of 315°
 - 2. Eight polygons defined by myself and three fellow classmates (two per person) around the same reference volcanic edifice displayed at a scale of 1:3000 (Figure 15), first in the shaded relief map with azimuth of 0°, then with an azimuth of 315°



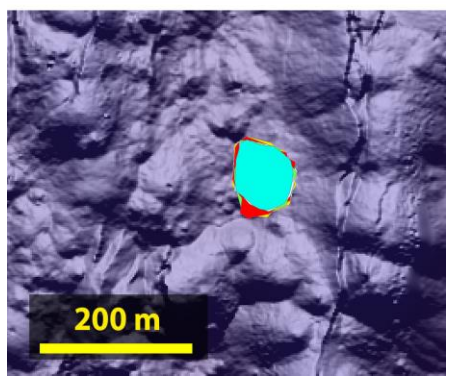


Figure 15: top) reference edifice revealed; **bottom**) multiple polygons defined over reference edifice in *ArcMAP*

(ii) Base depth determination: The third challenge I faced in estimating volumes of volcanic edifices is determining what base depth to use to calculate the height of a edifice. To calculate an edifice's volume requires an estimate of the shape of the seafloor before the volcanic construct was emplaced. To evaluate this uncertainty, I compared volumes calculated for edifices located within unit N2 using five base depths. I chose the following base depths after extended discussion with my three advisors:

- 1. The minimum depth of the individual edifice
- 2. The minimum depth of the unit containing the edifice
- 3. The mean depth of the unit containing the edifice
- 4. The mean of the minimum depths of all edifices contained within the unit containing the edifice
- 5. The minimum of the minimum depths of all edifices contained within the unit containing the edifice

5. Results

5.1 Results of uncertainty analysis

The 14 polygons defined around a reference volcanic edifice, by the methods described in section 4.7, yield a standard deviation that is 1.7% of the average calculated volume for this edifice (table 1). When plotted on any of the charts included here, this sigma value would cause none of the results to overlap, regardless of the y-axis value. This suggests that the uncertainty in volume calculations that results from the inconsistent user-definition of volcanic perimeters is not only acceptable for the reference volcanic edifice tested, but is invariant regardless of scale.

Of the five base depths (listed in the previous section) used to determine N2 volcanic edifice mean height (Figure 16), and subsequently volcanic edifice volume, two yield abundant negative values: the mean depth of the unit containing the edifice (calculated negative volumes=111) and the mean of the minimum depths of all edifices contained within the unit (calculated negative volumes=81). Because volume cannot be negative, these two base depth methods are not appropriate for this analysis. Of the remaining three base depth methods, two provide strikingly similar values: the minimum unit depth and the minimum of the minimum

User initials,			
azimuth, # of			
points	Area	avgz-minz	Volume
AM0	5677	23.360317	132616.5
JF0	5290	24.563709	129942
TL0	5477	23.96314	131246.1
WJ0	5211	24.538479	127870
KM0			
AM315	5568	23.834088	132708.2
JF315	5475	24.663244	135031.3
TL315	5320	24.345864	129520
WJ315	5477	23.866881	130718.9
KM315			
WJ0-8	5662	25.552172	144676.4
WJ0-16	5420	25.706121	139327.2
WJ0-24	5275	25.921293	136734.8
WJ315-8	5450	26.25641	143097.4
WJ315-16	5378	24.957839	134223.3
WJ315-24	5647	25.435001	143631.5
	stdev		
average volume	volume		
131206.6297	2226.038		

Table 1: values extracted by classmates for area, mean height, and volume. See text for explanation.

depths of all edifices contained within the unit. But as figure 17 clearly illustrates, units can tilt significantly from horizontal. Using a unit minimum depth or a minimum of the minimum depths

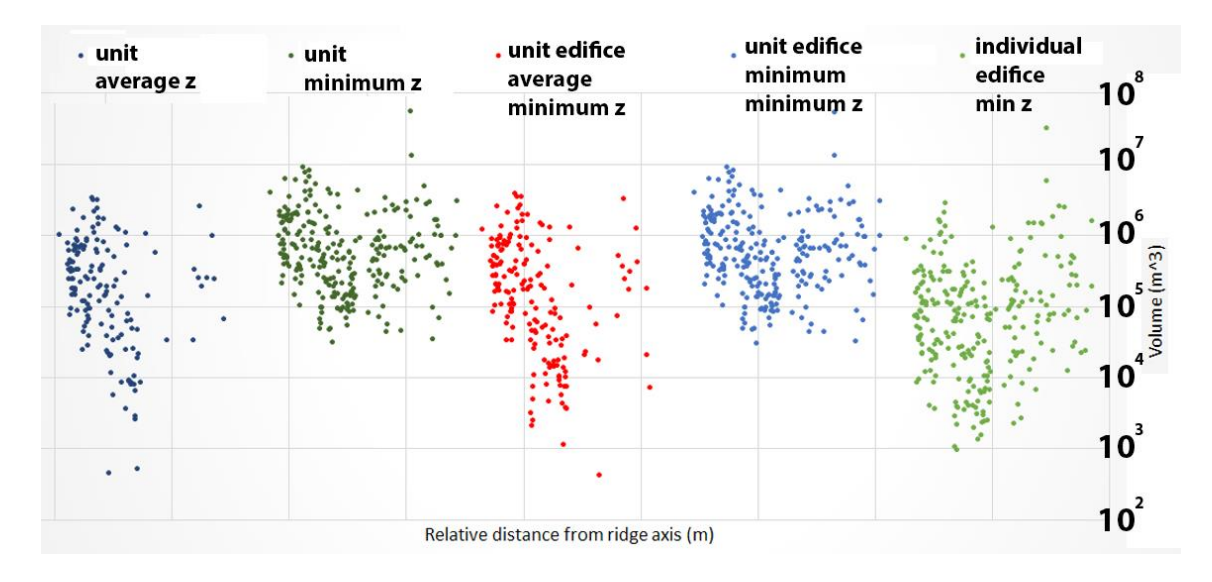


Figure 16: Base depth uncertainty analyses: five plots, each of the same individual edifice volumes from N2, each calculated using one of the five different base depths listed above the chart. Within each plot, volumes are plotted against relative distance from the ridge axis.

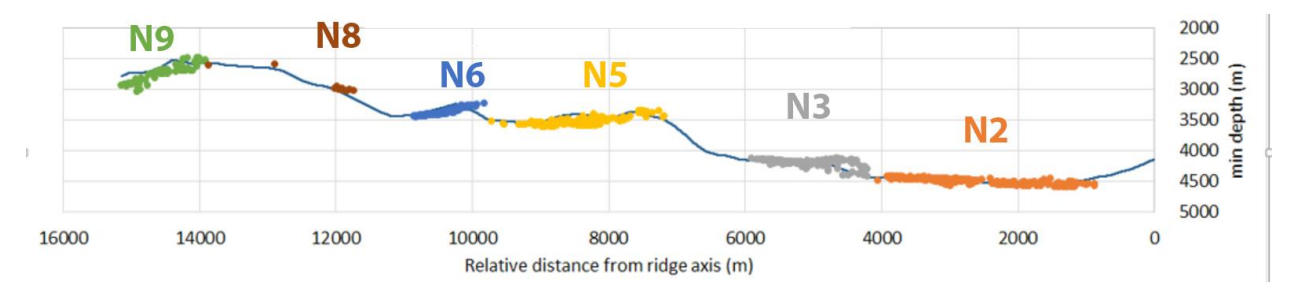


Figure 17: Minimum depth of each volcanic edifice plotted against the relative distance from the ridge axis. The volcanic edifices from different units are distinguished by color. The blue line is a profile taken down the center of the North swath.

of the edifices contained within that unit can lead to disproportionately higher volumes calculated for edifices based in more elevated portions of the unit. This trend is reflected in figure 17, even though the unit with which I performed the base depth uncertainty analysis (N2) shows the least variation in depth relative to the other north units.

5.2 Results of bathymetric analysis

Results of the bathymetric analysis allow for the distributions of individual hummock volumes of each unit to be compared. Only distinct hummocks were considered to be volcanic edifices in the box and whisker plots in figure 21. Figure 21 shows that C7, C8, C9, S3, S6, and N6 contain no volcanic edifices, and that volcanic edifice volumes for the remaining units vary by greater than three orders of magnitude.

Results also allow for a comparison of unit totals for volcanic volume, volcanic volume per unit area, and volcanic area (area covered by volcanic edifices) per unit area. Results vary depending significantly on what are considered to be edifices. Whether or not seamounts are considered volcanic edifices appears to make little difference in the relative volcanic edifice volume estimations of each unit. However, volume estimations differ significantly between analyses that consider ridges and hummocks to be volcanic edifices and those that only consider hummocks.

When only distinct hummocks are considered volcanic edifices: unit S1 contains the greatest total volcanic volume (\sim 1.8 x 10⁸ m³), followed by unit C5 (\sim 1.2 x 10⁸ m³), and then unit N2 (\sim 1.1 x 10⁸ m³) (Figure 18a and b); unit C2 contains the greatest total volcanic volume per unit area (\sim 50 m), followed by unit S1 (\sim 38 m), and then unit C5 (\sim 32 m) (Figure 19a and b); unit C2 contains the greatest volcanic area per unit area (\sim 0.75), followed by S1 (\sim 0.74), and then N2 and C6 (both \sim 0.59) (Figure 20).

When ridges and distinct hummocks that are not part of a ridge are considered volcanic edifices: unit C5 contains the greatest total volcanic volume (\sim 1.2 x 10^9 m³), followed by unit S1 (\sim 2.3 x 10^8 m³), and then unit N5 (\sim 1.5 x 10^8 m³) (Figure 18a and b); unit C5 contains the greatest total volcanic volume per unit area (\sim 330 m), followed by units C5 and C4 (\sim 150 m), and then unit N9 (\sim 40 m) (Figure 19a and b); units C5, C4, and C2 contain the greatest volcanic area per unit area (1.0), followed by S1 (\sim 0.79), and then N2 (\sim 0.63) (Figure 20).

When seamounts and distinct hummocks that are not part of a ridge are considered volcanic edifices: units S1 and N5 contain the greatest total volcanic volume (\sim 1.8 x 10⁸ m³), followed by unit N2 (\sim 1.7 x 10⁸ m³), and then unit C5 (\sim 1.1 x 10⁸ m³) (Figure 18a and b); unit C2 contains the greatest total volcanic volume per unit area (\sim 49 m), followed by unit S1 (\sim 38 m), and then unit C5 (\sim 32 m) (Figure 19a and b); unit C2 contains the greatest volcanic area per unit area (.75), followed by S1 (\sim 0.74), and then N2 (\sim 0.64) (Figure 20).

When seamounts, ridges, and distinct hummocks that are not part of a ridge are considered volcanic edifices: unit C5 contains the greatest total volcanic volume (\sim 1.2 x 10⁹ m³), followed by unit S1 (\sim 2.3 x 10⁸ m³), and then unit N5 (\sim 1.8 x 10⁸ m³) (Figure 18a and b); unit C5 contains the greatest total volcanic volume per unit area (\sim 330 m), followed by units C5 and C4 (\sim 150 m), and then unit S1 (\sim 50 m) (Figure 19a and b); units C5, C4, and C2 contain the greatest volcanic area per unit area (1.0), followed by S1 (\sim 0.79), and then N2 (\sim 0.68) (Figure 20).

Figure 21 shows box and whisker plots of the distribution of individual hummock volumes, plotted by unit. Most obvious is the absence of hummocks from several units, many of which are adjacent to units containing hummocks. In addition, it is clear that in the north and in the south, the distributions of individual hummock volumes of several units containing hummocks differ significantly (no overlap between "boxes" of box and whisker plots).

For an interpretation of these results, see Discussion section.

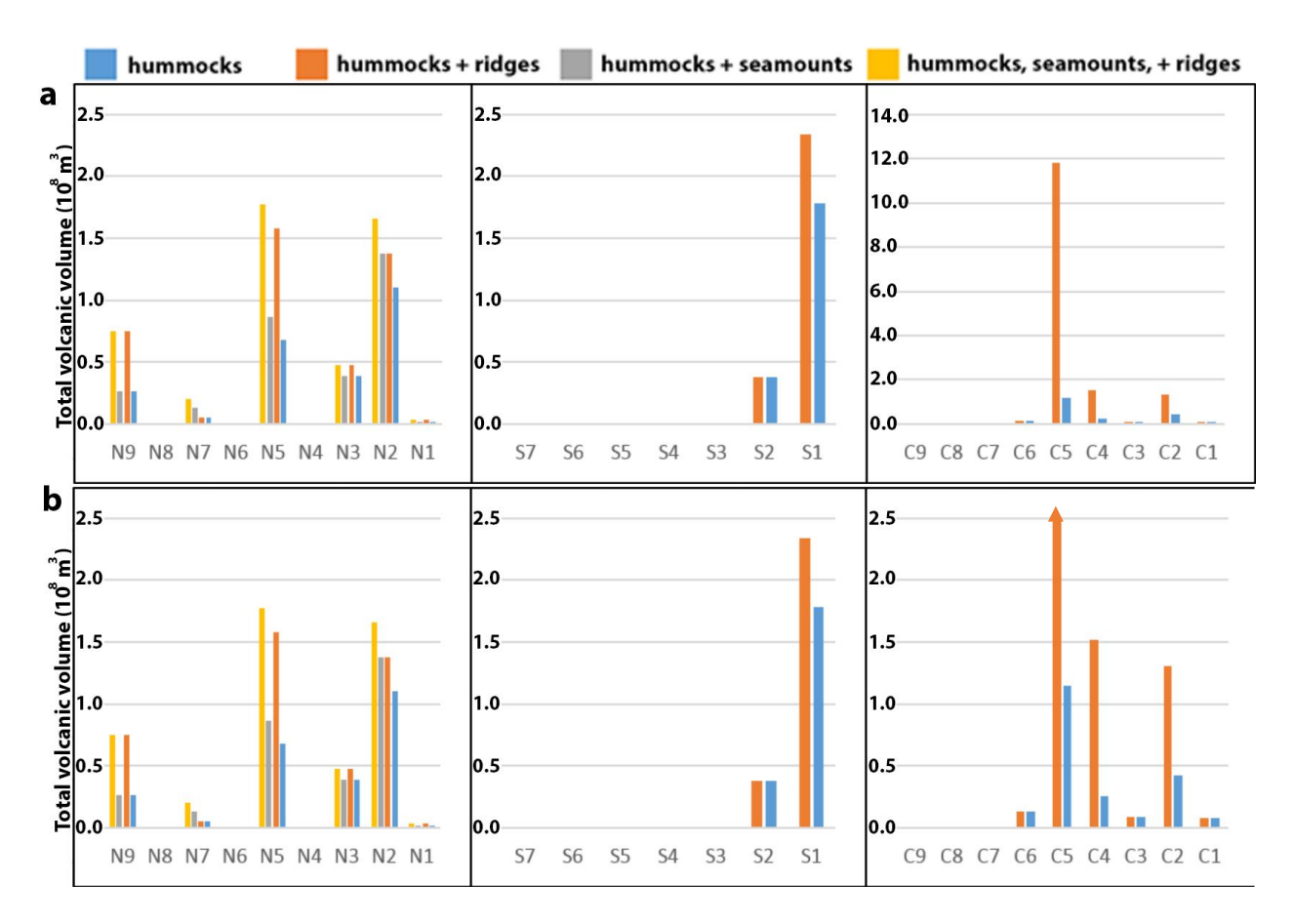


Figure 18: Total volcanic volume (m³), by unit. Seamounts were not found in south units or central units, so for these units the "hummocks + ridges" and "hummocks, seamounts, + ridges" datasets, and the "hummocks" and "hummocks + seamounts" datasets are identical. For this reason, only the "hummocks" and "hummocks + ridges" datasets are shown for these units. **a)** Vertical scale of north and south units is different from central units; **b)** vertical scale is the same for all units.

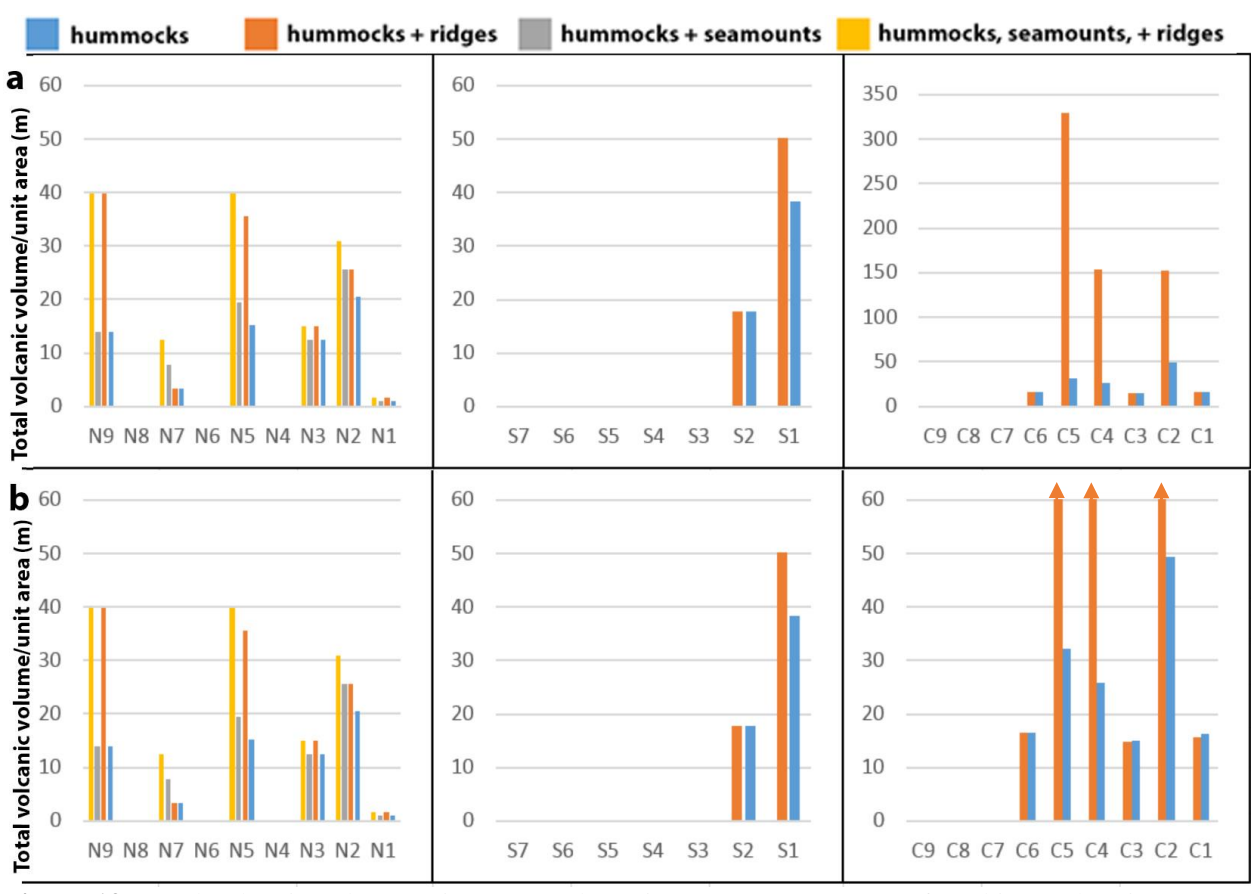


Figure 19: Total volcanic volume/unit area, (m) by unit. Seamounts were not found in south units or central units, so for these units the "hummocks + ridges" and "hummocks, seamounts, + ridges" datasets, and the "hummocks" and "hummocks + seamounts" datasets are identical. For this reason, only the "hummocks" and "hummocks + ridges" datasets are shown for these units. **a)** Vertical scale of north and south units is different from central units; **b)** vertical scale is the same for all units.

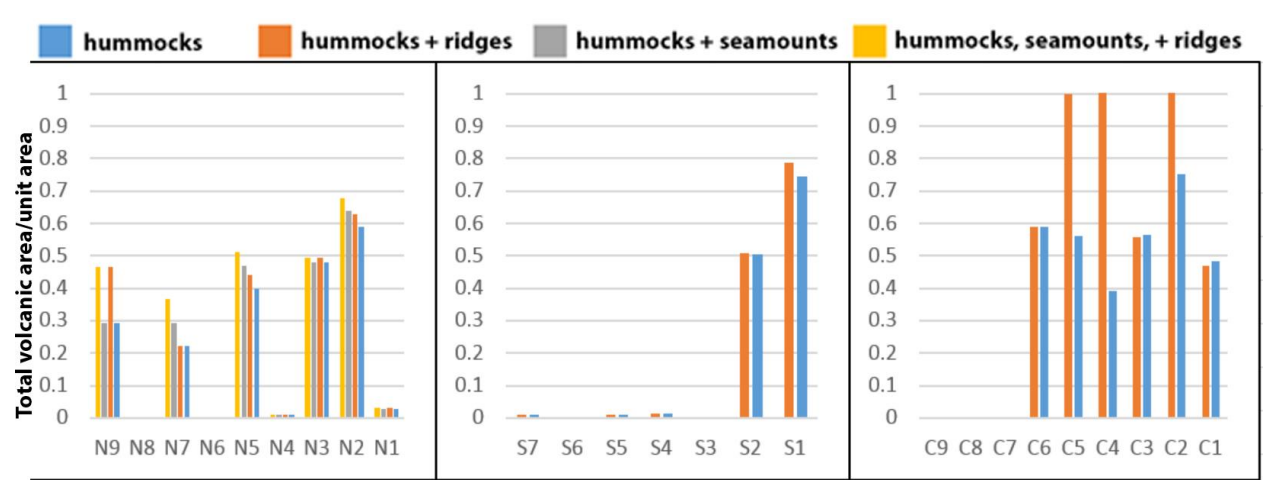


Figure 20: Total volcanic area/unit area, by unit. Seamounts were not found in south units or central units, so for these units the "hummocks + ridges" and "hummocks, seamounts, + ridges" datasets, and the

"hummocks" and "hummocks + seamounts" datasets are identical. For this reason, only the "hummocks" and "hummocks + ridges" datasets are shown for these units. a) Vertical scale is the same for north and south units; b) vertical scale the same for all units.

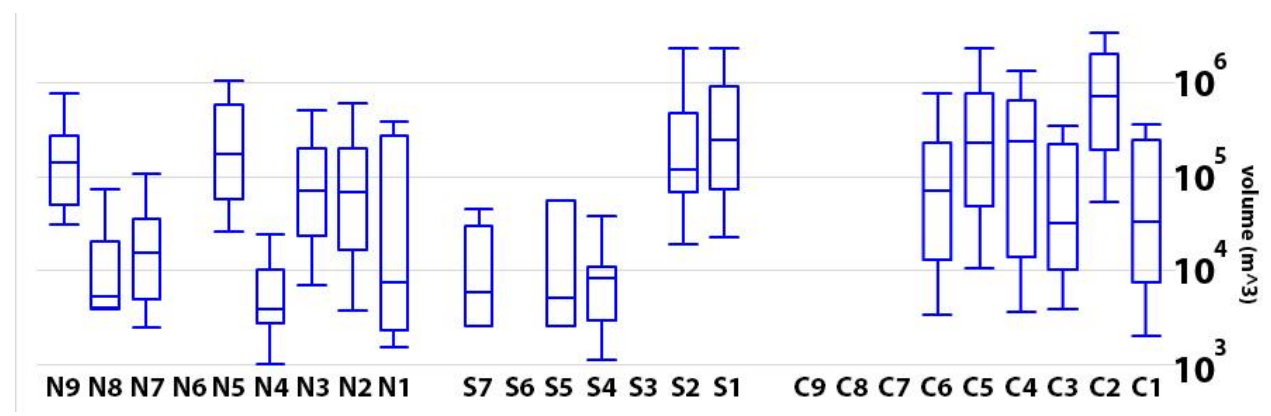


Figure 21: box and whisker plots of distribution of individual hummock volumes, plotted by unit. Each horizontal bar represents, from top to bottom, the 90th, 75th, 50th, 25th, and 10th datum, respectively.

6. Discussion

My first hypothesis is that within the area of study, magma supply increases from north to south along the ridge axis. Consistent with the regional bathymetric trend of increasing ridge axis elevation from north to south (Figure 5), the analysis of volcanic edifices in high-resolution bathymetry maps reveals a significantly stronger magmatic signal in the south swath than in the north swath. There is greater volume of material contained in the S1 unit volcanic edifices than in any unit from the north swath both before (Figure 18), and after normalizing volcanic volume by unit area (Figure 19). Additionally, although the proportion of north swath to south swath volcanic volume increases when entire ridges are considered, the S1 unit yet remains the most volcanic unit contained in the two areas. The S1 unit is also the unit with the greatest proportion of volcanic coverage of all the north and south units (Figure 20), although several units in the north are nearly as covered by volcanic edifices as S1, and the case for greater volcanism in the south than in the north is evidenced most strongly by total volcanic volume before and after normalization by unit area.

It is unclear whether my first hypothesis—that magma supply increases from north to south along the ridge—is consistent with results from C1-C6. When ridges are ignored and only distinct hummocks are considered, S1 has the greatest total volcanic volume before normalization by unit area (Figure 18), and is second only to unit C2 after normalization by unit area (Figure 19). However, this result deserves qualification: of all the units analyzed in this study, C2 is one of the smallest by area, and the C1-C6 unit boundaries were among the most uncertain and subjectively determined. Boundaries could have been reasonably defined for the units C1-C6 that would have resulted in S1 having the greatest total volcanic volume of all the units analyzed, before and after normalization by area.

When entire ridges are considered as volcanic edifices, total volcanic volume in unit C5 is an order of magnitude greater than in any other unit before normalization by unit area, with S1 a distant second (Figure 18); and when normalized by unit area, S1 is surpassed in terms of total volcanic volume by units C2, C4, and C5 (Figure 19). It should be noted however that units C2, C4, and C5 have each been interpreted as consisting entirely of a single massive ridge. This result showcases the dependence of this study on the scale of the volcanic edifices considered, and similarly on the interpretation of what qualifies as a volcanic edifice.

Unit C5 provides an example of the difficulties I encountered and the uncertainties I faced for edifices composed entirely of volcanic material. I attempted to base my interpretations of volcanic edifices on published interpretations, but in all my reading I could find no volcanic edifice quite like the massive ridge in C5 (Figure 14). It is also worth noting that the ridge in unit C5 is unique to the bathymetric maps analyzed in this study. The triangular cross section of the ridge (Figure 14a) would not result from rounded hummocks piled and coalesced, so an interpretation of the ridge as purely volcanic requires additional explanation. Perhaps one or both of the flanks of the "ridge" are actually fault scarps underlying



Figure 22: Towcam photo of the seafloor showing shattered pillow basalts (as indicated by rounded, striated surfaces) forming a slope, consistent with mass wasting of a ridge of volcanic origin. The two green dots in the center of the image are 30 cm apart. The precise location of the TowCam system relative to the ship is difficult to determine but this area corresponds to swath 184.

hummocks formed by lateral flows or vertical feeder pipes that can intersect a fault surface at MORs (Smith and Cann, 1993). Such an edifice would not be unique to the maps analyzed in this study, as scarps underlying hummocks can be found in the north units N3, N4, and possibly N8. However, the regional bathymetry map shows the ridge in unit C5 continuing well south of C5 (Figure 5), so the interpretation that this ridge is a tectonic edifice seems unlikely. Mass wasting could possibly explain the triangular cross section observed. Concave scars atop the ridge support the interpretation of mass wasting, as do TowCam photos taken within or nearby the swath (Figure 22).

Even if mass wasting is responsible for the triangular cross section shape, the question remains how much significance we should impute to the total volcanic volume analysis that considers ridges volcanic edifices, versus the analysis that only considers distinct hummocks. One possible interpretation is that the ridge in unit C5 consists of both intrusive and extrusive material. Pillow basalt layers at MORs can be as thin as 300 m (Nicolas and Boudier, 2003), with the material below crystallized from magma that never reached the seafloor. Considering that the unit C5 ridge shows over 500 m of relief (Figure 14a), it is reasonable to assume that a total volcanic volume estimate that treats such an edifice as purely volcanic will overestimate the magma supply beneath the ridge.

For these reasons, I am inclined to consider the comparison between the south units and C1-C6 units inconclusive. The far more certain result is that volumetrically, units from both the south units and C1-C6 units display significantly more volcanism than any unit from the north swath, consistent with my first hypothesis that magma supply increases from north to south along the ridge. Although anticipated, this is a striking result nonetheless. Both classic and more modern theories of MOR spreading hold that the more amagmatic portions of a ridge will accommodate spreading through numerous normal faults and long-lived detachment faults (Buck et al., 2005; Escartin et al., 2008; Buck et al., 2005; Tucholke et al., 2008). Yet in the area of study, the long-lived detachment faults and associated core complexes are located directly off axis from the most magmatic portion of the ridge (Figure 5).

My second hypothesis is that magma supply has remained constant over time along the entire ridge. Although in terms of individual volcanic edifice volume the C1-C6 units in the figure 21 box and whisker plots appear consistent within uncertainty, the box and whisker plots for the south and north units provide strong evidence that magma supply is not constant through time at all locations along the ridge. Individual volcanic edifice volume distributions are significantly higher in units N9, N5, N3, and N2, and lower in units N8, N7, N6, and N4. Units N8, N6, and N4 are almost devoid of volcanic material entirely (Figures 18-21), and may represent periods of purely amagmatic spreading. In addition, these amagmatic units are located in space between units with obvious abundant magmatism (N2, N3, N5, N9), a result that suggests that magma supply beneath the ridge in the north of the area of study has fluctuated over the ~700 ka (based on 21mm/yr spreading rate (Perfit and Chadwick, 1998), 14 km long map) represented in the northern high-resolution bathymetry map. Even more strikingly amagmatic in appearance are the south swath units west of S2, where volcanism appears almost entirely absent (Figures 18-21), and the central units C7, C8, and C9. The relationship between the apparently amagmatic C7-C9 swaths and very magmatic C1-C6 swaths just to the east mirrors the relationship between the south swath units west of S2 and the units S2 and S1. Clues to this similarity can be found in C8 and S6, which display surfaces devoid of volcanism and smooth but for conspicuous corrugations—evidently the surfaces of long-lived detachment faults (Figure 11). All these results suggest that detachment faults are more complex, their formation less related to reduced magma supply than we once thought.

7. Acknowledgements

I would like to thank my three advisors for their constant support and accessibility throughout this project. I am especially grateful to Laurent Montesi for his consistent guidance and for his lucid explanations of various aspects of MOR geology (without which I would have made little sense of the literature I read and the research I conducted over the past year). I cannot thank Wen-lu Zhu enough for inviting me to participate on the KN 210-05 cruise—an experience I will always recall fondly—and for her substantial guidance in the formation of my project in the early fall of 2013. I would like to thank Debbie Smith for regularly sharing with me her expertise on complex MORs, for her provision of critical source material, and for her impressive

contributions to MOR geology that made both the KN 210-05 cruise and this project possible. I would also like to thank Dana Yoerger and the technical support team for *Sentry* during the KN 210-05 cruise for their excellent on-site data processing and production of the netCDF files used in this study. Additionally, I am grateful to my fellow members of the KN 210-05 science party for their patience and generosity in acquainting me with MORs. Finally, I wish to acknowledge and thank the crew of the *R.V. Knorr*; the competence and professionalism with which they conducted themselves over the 40-day cruise contributed greatly to both the efforts and the morale of the science party.

References

- Bohnenstiehl, D., Kleinrock, M.C., 1999, Faulting and fault scaling on the median valley floor of the trans-Atlantic geotraverse (TAG) segment, ~260N on the Mid-Atlantic Ridge. J. Geophys. Res., 104, p. 29351-64
- Buck, W.R., Lavier, L.L., and Poliakov, A.N.B., 2005, Modes of faulting at mid-ocean ridges: Nature, 434, p. 719–723, doi:10.1038/nature03358.
- Colman, A., Sinton, J. M., White, S. M., McClinton, J. T., Bowles, J. A., Rubin, K. H., Behn, M. D., Cushman, B., Eason, D. E., Gregg, T. K. P., Gronvold, K., Hidalgo, S., Howell, J., Neill, O., Russo, R., 2012, Effects of variable magma supply on mid-ocean ridge eruptions: Constraints from mapped lava flow fields along the Galápagos Spreading Center, Geochem. Geophys. Geosyst., 13, Q08014, doi:10.1029/2012GC004163.
- Escartín, J., Smith, D.K., Cann, J., Schouten, H., Langmuir, C.H., and Escrig, S., 2008, Central role of detachment faults in accretion of slow-spreading oceanic lithosphere: Nature, 455, doi:10.1038/nature07333.
- Fujiwara, Toshiya, Jian Lin, Takeshi Matsumoto, Peter B. Kelemen, Brian E. Tucholke, and John F. Casey, 2003, Crustal Evolution of the Mid-Atlantic Ridge Near the Fifteen-Twenty Fracture Zone in the Last 5 Ma. Geochemistry, Geophysics, Geosystems. 4.3. Print.
- MacDonald, K. C., Scheirer, D. S., Carbotte, S. M., 1991, Mid-Ocean Ridges: Discontinuities, Segments and Giant Cracks. *Science*, New Series, 253, No. 5023 (Aug. 30, 1991), pp. 986-994
- Neumann, G. A., and D. W. Forsyth, 1993, The paradox of the axial profile: Isostatic compensation along the axis of the Mid-Atlantic Ridge?, J. Geophys. Res., 98, 17891-17911.
- Nicolas, A., Boudier, F., 2003, Where ophiolites come from and what they tell us. Geological Society of America Special Papers, 373, p. 137-152,
- Nicolas, A., 1995, The Mid-Oceanic Ridges: Mountains Below Sea Level. Berlin Heidelberg: Springer-Verlag.
- Perfit, M. R., and W. W. Chadwick, 1998, Magmatism at midocean ridges: Constraints from volcanological and geochemical investigations, in Faulting and Magmatism at Mid-ocean Ridges, Geophys. Monogr. Ser., 106, edited by W. R. Buck, pp. 59–116, AGU, Washington, D. C.
- Scholz, C. H., and Cowie, P. A., 1990, Determinatin of total strain from faulting using slip measurements, Nature, 346, p 837-839

- Searle, R.C., Murton, B.J., Achenback, K., LeBas, T., Tivey, M., Yeo, I., Cormier, M.H., Carlut, J., Ferreira, P., Mallows, C., Morris, K., Schroth, N., van Calsteren, P., Waters, C., 2010, Structure and development of an axial volcanic ridge: Mid-Atlantic Ridge, 45°N, Earth and Planetary Science Letters, 299, p. 228-241
- Smith, D. K. and Cann, J. R., 1993, Building the crust at the Mid-Atlantic Ridge, Nature, 365, p. 707-714
- Smith, D. K., J. Escartin, H. Schouten, and J. R. Cann, 2008, Fault rotation and core complex formation: Significant processes in seafloor formation at slow-spreading mid-ocean ridges (Mid-Atlantic Ridge, 13°–15°N), Geochem. Geophys. Geosyst., 9, Q03003, doi:10.1029/2007GC001699.
- Smith, D. K., J. Escartin, M. Cannat, M. Tolstoy, C. G. Fox, D. Bohnenstiehl, and S. Bazin, 2003, Spatial and temporal distribution of seismicity along the northern Mid-Atlantic Ridge (15°–35°N), J. Geophys. Res., 108/2167, doi:10.1029/2002JB001964.
- Smith, D. K., Schouten, H., Dick, H. J. B., Cann J. R., Salters, V., Marshall, H., Ji, F., Yoeger, D., Sanflippo, A., Parnell-Turner, R., Palmiotto, C., Zheleznov, A., Bai, H., Urann, B., Junkin, W., Dick, S., Sulanowska, M., Lemmond, P., Curry, S., 2013, Development of different modes of detachment faulting, 16.5°N at the Mid-Atlantic Ridge, Interridge News. Vol. 22, December, 2013, p. 21-26
- Smith, D. K., Schouten, H., Dick, H. J. B., Cann J. R., Salters, V., Marshall, H., Ji, F., Yoeger, D., Sanflippo, A., Parnell-Turner, R., Palmiotto, C., Zheleznov, A., Bai, H., Urann, B., Junkin, W., Dick, S., Sulanowska, M., Lemmond, P., Curry, S., 2013, Development of detachment faults at intermediate magma supply, Cruise Report, KN210-05
- Smith, D.K., and Cann, J.R., Constructing the upper crust of the Mid-Atlantic Ridge: A reinterpretation based on the Puna Ridge, Kilauea Volcano, J. Geophys. Res., 104, 25,379-25,399, 1999.
- Staudigel, H., 2014, 4.16 Chemical Fluxes from Hydrothermal Alteration of the Oceanic Crust, In Treatise on Geochemistry (Second Edition), edited by Heinrich D. Holland and Karl K. Turekian, Elsevier, Oxford, Pages 583-606, ISBN 9780080983004, doi:10.1016/B978-0-08-095975-7.00318-1.
- Thibaud, R., P. Gente, and M. Maia, 1998, A systematic analysis of the Mid-Atlantic Ridge morphology and gravity between 15°N and 40°N: Constraints of the thermal structure, J. Geophys. Res., 103, 24,223–24,243.
- Tucholke, B.E., Behn, M.D., Buck, R., and Lin, J., 2008, The role of melt supply in oceanic detachment faulting and formation of megamullions: Geology, 36, p. 455–458, doi:10.1130/G24639A.1.